PAPER • OPEN ACCESS

Nonlocal ultrafast demagnetization dynamics of Co/Pt multilayers by optical field enhancement

New Journal of Physics
The open access journal at the forefront of physics

Deutsche Physikalische Gesellschaft DPG
IOP Institute of Physics

Published in partnership with: Deutsche Physikalische Gesellschaft and the Institute of Physics

OPEN ACCESS

RECEIVED
22 August 2014

REVISED
20 January 2015

ACCEPTED FOR PUBLICATION
23 February 2015

PUBLISHED
31 March 2015

PAPER

Nonlocal ultrafast demagnetization dynamics of Co/Pt multilayers by optical field enhancement

C von Korff Schmising[1], M Giovannella[1], D Weder[1], S Schaffert[1], J L Webb[3] and S Eisebitt[1,2,3]

[1] Insitut für Optik und Atomare Physik, Technische Universität Berlin, 10623 Berlin, Germany
[2] Helmholtz-Zentrum Berlin für Materialien und Energie GmbH, Hahn-Meitner-Platz 1, D-14109 Berlin, Germany
[3] Division of Synchrotron Radiation Research, Department of Physics, Lund University, S-22100 Lund, Sweden

E-mail: c.vonkorffschmising@tu-berlin.de

Keywords: ultrafast demagnetization, plasmonic, nano structure

Supplementary material for this article is available online

Abstract

The influence on ultrafast demagnetization dynamics of metallic nano-structured gratings deposited on thin films of magnetic Co/Pt multilayers is investigated by the time-resolved optical Kerr effect. Depending on the polarization of the pump pulse, a pronounced enhancement of the demagnetization amplitude is found. Calculation of the inhomogeneous optical field distribution due to plasmon interaction and time-dependent solutions of the coupled electron, lattice, and spin temperatures in two dimensions show good agreement with the experimental data, as well as giving evidence of non-local demagnetization dynamics due to electron diffusion.

1. Introduction

Advances in the field of ultrafast demagnetization dynamics have recently been driven by intelligent design of sample geometries, leading to a controlled response of the magnetization on femtosecond time scales [1–3] and to all-optical helicity-dependent switching [4, 5]. Besides tailoring structural inhomogeneities by assemblies of (anti-)ferromagnetic/metallic or rare-earth/transition metal multilayers, recent studies of magnetic heterogeneous systems have revealed how ultrafast transport-related magnetization processes [6] are influenced by magnetic domain structures [7, 8]. Furthermore, Fourier transform holography allowed a direct visualization of the femtosecond transient magnetization after a localized laser excitation and gave evidence for non-local magnetization dynamics within a magnetic domain network [9]. Tailoring magnetic samples to control the localization and enhancement of the optical excitation is being explored for applications in heat-assisted magnetic recording [10, 11], with a new found interest for all-optical- switching techniques with nanoscale bit-sizes. So far, however, the influence of such plasmonic nanostructures on the femtosecond temporal and nanometre spatial evolution of the magnetization has remained mostly unexplored; the fundamental spatial limit of confining optical-induced magnetization processes is unknown.

Here, we explore via the ultrafast time-resolved optical Kerr effect how metallic nano structured gratings influence the amplitude as well as temporal and spatial evolution of magnetization dynamics of thin Co/Pt multilayer films. Experimental results showing a polarization-dependent enhancement of the demagnetization are corroborated by calculations of the electric field distribution as well as simulations with a nonlocal extension of the time- and space-dependent three temperature model (TTM) [12], describing the equilibration of electron, lattice, and spin degrees of freedom. Within this model, we illustrate strategies of how engineered metallic nanostructures allow us to control ultrafast electron diffusion, resulting in non-local ultrafast magnetization dynamics.

2. Experimental methods

A Co/Pt multilayer sample with a composition of Ta(20 Å)/Pt(30 Å)/$[$Co(8 Å)/Pt(14 Å)$]_{11}$/Pt(6 Å) was deposited on a silicon wafer via magnetron sputtering; its corresponding hysteresis loop is shown in figure 1(b).

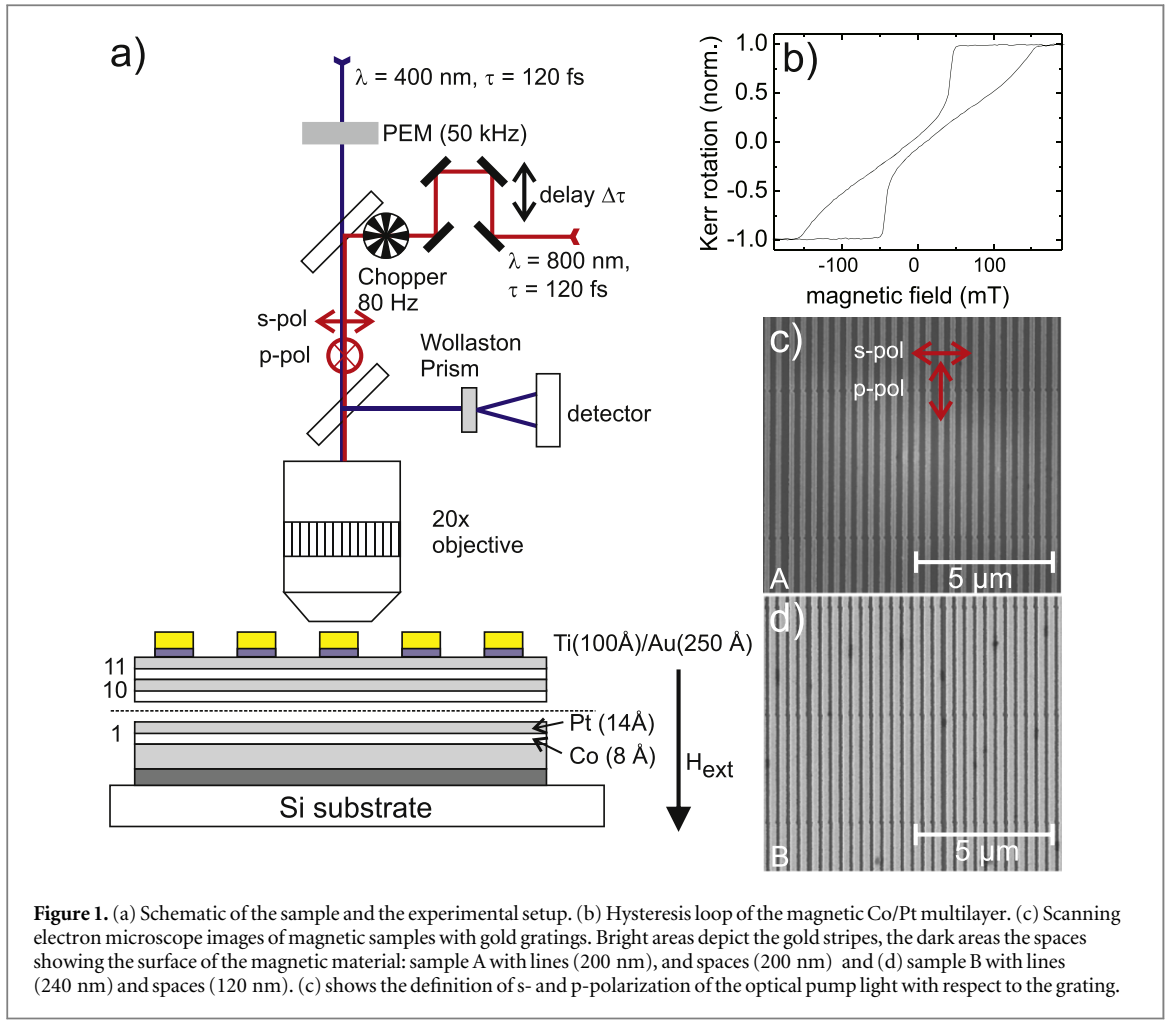

Figure 1. (a) Schematic of the sample and the experimental setup. (b) Hysteresis loop of the magnetic Co/Pt multilayer. (c) Scanning electron microscope images of magnetic samples with gold gratings. Bright areas depict the gold stripes, the dark areas the spaces showing the surface of the magnetic material: sample A with lines (200 nm), and spaces (200 nm) and (d) sample B with lines (240 nm) and spaces (120 nm). (c) shows the definition of s- and p-polarization of the optical pump light with respect to the grating.

Gold/titanium gratings with lateral dimensions of $100 \times 100\ \mu m^2$ and a thickness of 35 nm (Ti(250 Å)/Au (100 Å) were patterned on the magnetic surface by electron beam lithography with deposition by thermal evaporation under high vacuum. Scanning electron images of sample A with lines and spaces (200 nm/200 nm) and sample B with lines and spaces (240 nm/120 nm) are shown in figures 1(c) and (d).

The ultrafast demagnetization dynamics were studied by a two-colour time-resolved magneto optical Kerr setup in polar geometry, as schematically shown in figure 1(a). The Co/Pt multilayer is magnetically saturated by an external static magnetic field H_{ext} of 300 mT. Near-infrared light pulses, centred at a wavelength of $\lambda = 800$ nm, with a temporal width of 120 fs and a repetition rate of 545 kHz, excite the sample for varying time delays $\Delta\tau$. The polarization of the pump pulses is aligned either parallel (p-polarization) or perpendicular (s-polarization) with respect to the gold lines and spaces (see figure 1(c)). Additionally, the pump pulses are mechanically modulated with 80 Hz. The synchronized probe pulses are derived by frequency doubling ($\lambda = 400$ nm) and modulated with a photoelastic modulator (PEM) at 50 kHz. The beam diameters (full width at half maximum (FWHM)) in the focal plane of a 20x infinity-corrected microscope objective were determined by a knife edge scan and amounted to 2.7 x 2.5 μm^2 ($\lambda = 400$ nm) and 6.7 x 7 μm^2 ($\lambda = 800$ nm) in the x- and y-direction, respectively. After reflection of the probe beam its s- and p-components are split by a Wollaston prism and detected by a balanced photo-diode. For further noise reduction the difference signal is processed by a double lock-in technique, modulated with the frequency of the PEM, and the frequency of the mechanical chopper. Note that this low-noise measurement technique employing lock-in detection does not allow us to infer absolute demagnetization rates. Dispersion of the probe beam in the microscope objective, PEM, and polarizing optics is pre-compensated by a prism compressor; a cross-correlation measurement determines the overall temporal resolution at the sample to 180 fs.

A commercial-grade simulator based on the finite-difference time-domain method [13] was used to calculate the enhanced electric field E distribution due to the metallic grating after excitation with $\lambda = 800$ nm pump light pulses under normal incidence. The absorbed power is calculated according to $P_{abs} = -0.5\omega|E|^2\Im(\epsilon)$, with ω as the circular frequency of the light field and $\Im(\epsilon)$ the complex part of the

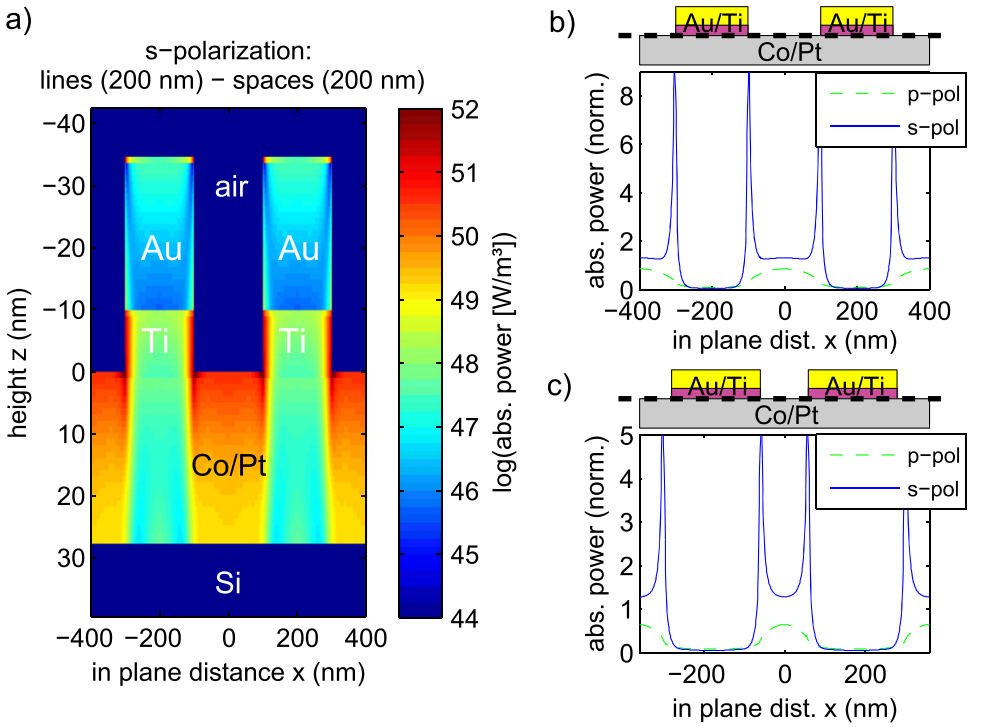

Figure 2. (a) Two-dimensional calculation of absorbed power for sample A and an incident fluence of f =4 mJ cm^{-2} on a logarithmic scale. The highest absorbed power corresponds to 1E23 W m^{-3}. One observes a strong enhanced absorption at the edges of the grating, extending several nanometres into the magnetic film. (b) Absorption cross section at the surface of the magnetic film (dashed black line in sample schematic) normalized to the absorption profile without Ti/Au grating. One observes a distinct difference in the excitation profile, depending on the incoming polarization for sample A and (c) for sample B.

dielectric permittivity (see appendix A2). The calculation was performed for a single unit cell (i.e., one line, one space) with periodic boundary conditions in lateral dimension x and with absorbing perfectly matched layers at the top and bottom of the structure in the z direction. Convergence was carefully tested by changing the maximum edge length of the triangular mesh of the calculation between 5 Å and 2 Å. Calculations of structures with infinitely sharp Au edges were compared with rounded edges (radius 4.2 nm) and resulted in negligible differences in absorbed power. Figure 2 summarizes the results: (a) shows a two-dimensional plot of the absorbed power P_{abs} on a logarithmic scale for sample A and for s-polarized light with an excitation fluence of f =4 mJ cm^{-2}. One observes a pronounced enhanced absorption at the edges of the gold/titanium grating extending several nanometres into the magnetic layer. Figures 2(b) and (c) show the absorbed power at the surface of the Co/Pt multilayer normalized to the absorption without the Ti/Au grating. The very strong enhanced absorption at the edges very rapidly decays as a function of depth. Because the PEM modulates the polarization state of the probe beam, we assume a constant probe light intensity in the lateral plane between the gold stripes, penetrating the layer with an absorption length of 11 nm. Strong reflection and absorption minimizes the light field under the gold stripes. For s-polarization one observes an enhancement at the edges; p-polarized light shows a maximum P_{abs} between the gold stripes and minima at the edges.

3. Results and discussions

Figures 3(a)–(c) show the experimental results of the ultrafast evolution of the Kerr rotation after optical excitation. The left panel compares the results for the unstructured sample and sample A for s- and p-polarization. An initial ultrafast drop of the magnetization on the order of a few hundred femtoseconds (demagnetization time τ_{de}) is followed by a slower recovery (remagnetization time τ_{re}). On even longer time scales a further remagnetization is observed, which is attributed to heat diffusion processes. A quantitative analysis is reached by assuming the following functional dependence:

$$\frac{\Delta M}{M_0} = G(t) \otimes H(t)\left[\frac{A_1}{\sqrt{1 + t/t_0}} + A_2 \mathrm{e}^{-t/\tau_{\mathrm{de}}} + A_3 \mathrm{e}^{-t/\tau_{\mathrm{re}}}\right] \quad (1)$$

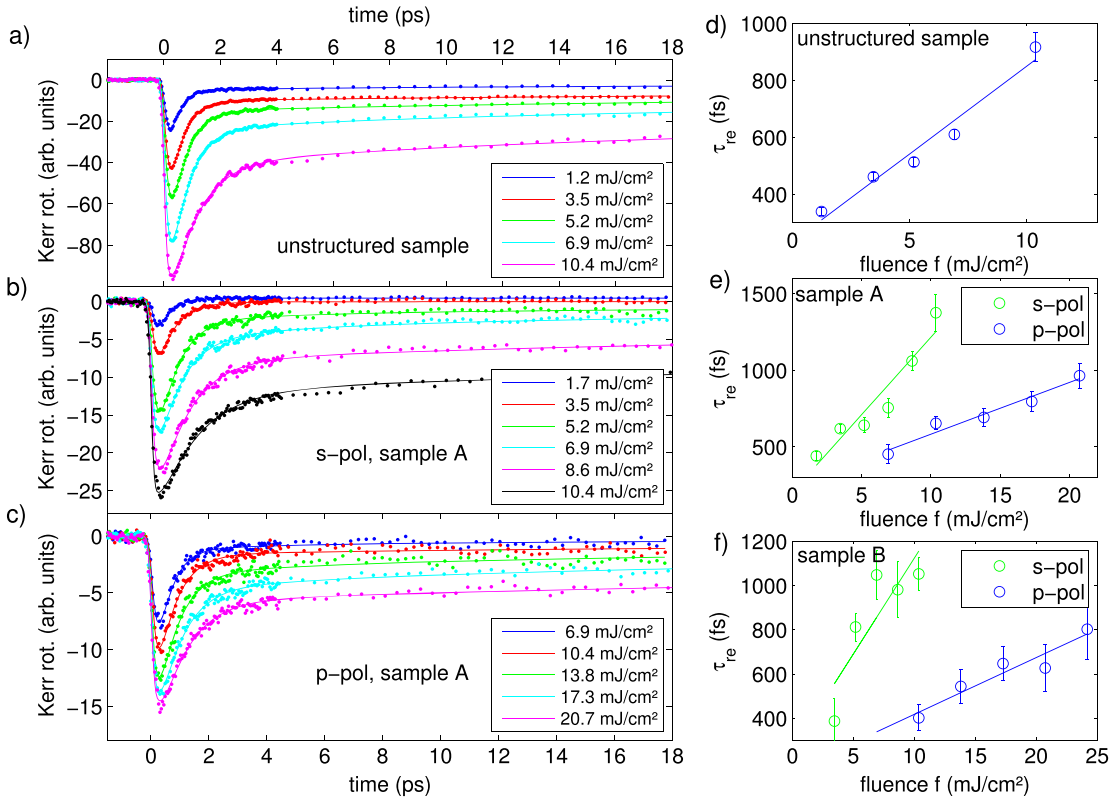

Figure 3. Experimental data of ultrafast evolution of the Kerr rotation as a function of time for different excitation fluences. The solid lines are the corresponding non-linear least square fits using equation (1). (a) Data for the unstructured magnetic sample, (b) for sample A and s-polarized excitation and (c) for sample A and p-polarized excitation. Remagnetization time constants, τ_{Re}, with their 1-σ error bars as a function of fluence, solid lines are linear least square fits (d) unstructured sample $\tau_{re} = 232 + 62 \cdot f$, $r^2 = 0.96$, (e) for sample A with s- and p-polarized excitation $\tau_{re,s} = 245 + 34 \cdot f$, $r^2 = 0.96$, $\tau_{re,p} = 205 + 101 \cdot f$, $r^2 = 0.90$ and (f) for sample B with s- and p-polarized excitation $\tau_{re,s} = 162 + 26 \cdot f$, $r^2 = 0.91$, $\tau_{re,p} = 256 + 87 \cdot f$, $r^2 = 0.72$. Note the different slopes.

and performing non-linear least square fits of the data. The re- and demagnetization times, τ_{re} and τ_{de}, respectively, are modelled by an exponential function; longer time scales are approximated by an inverse square-root function [1]. $H(t)$ is the Heaviside function, and the time resolution of the experiment is taken into account by performing a convolution with a Gaussian $G(t)$ with an FWHM of 180 fs.

Figures 3(d)–(f) show the remagnetization time, τ_{re}, as a function of the excitation fluence, f: while all curves show a linear relationship between remagnetization time and excitation fluence, the slopes depend on both the incoming pump polarization as well as the grating periodicity.

In passing we like to note that care has to taken when comparing extracted absolute de- and remagnetization time constants reported in the literature, as they will not only evidently depend on the phenomenological model used to describe the data [14], but also on the time range taken into account for fitting. In particular, slower remagnetization processes associated with heat diffusion can have a considerable influence on both τ_{re} and τ_{de}, in spite of being dominated by extrinsic properties like sample geometries and substrates. This also applies to the calculated confidence interval of the fitting routine, which tends to increase with increasing time range. A direct comparison of time constants is further complicated by the general observation that the magnetization dynamics is a function of the excitation fluence, a value often only known with a considerable uncertainty.

In the following we argue that the extracted remagnetization time constants, τ_{re}, are directly proportional to the amplitude of the demagnetization and therefore allow a quantitative comparison of the efficiency of the demagnetization process between unstructured and structured samples. Such an indirect calibration is necessary, because we detect light reflected both by the magnetic multilayer and the gold parts of the sample surface, which would lead to a systematic underestimation of the absolute Kerr rotation originating from the exposed parts of the magnetic multilayer. An experimental determination of the absolute scale of demagnetization is prevented by the lock-in technique as well as a large Faraday rotation induced in the microscope objective when alternating the external magnetic field. The linear increase of the extracted remagnetization time constants, τ_{re}, as a function of excitation fluence (shown in figures 3(d)–(f) has previously been demonstrated experimentally and has been predicted by atomistic Landau–Lifshitz–Bloch and Landau–Lifshitz–Gilbert approaches [15, 16], as well as by the microscopic TTM of Koopmans *et al* [17]. Because for

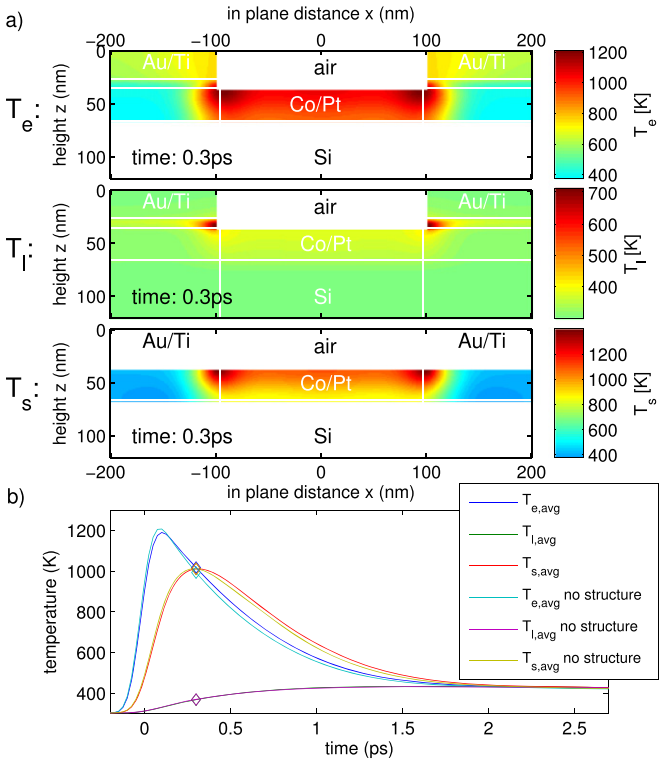

Figure 4. (a) Calculated solution of the three temperature model showing the electronic (T_e), lattice (T_l), and spin (T_s) temperatures at t = 300 fs for sample A and s-polarized excitation with 4 mJ cm^{-2}. At the edges of the grating, the spin system of the Co/Pt multilayer is locally heated to maximum temperatures. (b) Calculated temporal evolution of the integrated temperatures T_e, T_l, and T_s between −100 nm and 100 nm weighed with the exponential absorption profile of $\lambda = 400$ nm probe light. To reach the same amplitude of demagnetization with or without gold grating, the excitation fluence for the unstructured sample is scaled by a factor of 1.3. One observes a very subtle increase of τ_{de} by 10 fs as well as an increase of τ_{re} by 35 fs.

moderate excitation densities (<30 mJ cm^{-2}) the demagnetization scales linearly with fluence [12, 18] (see also figure 3), we conclude that the measured slope of τ_{re} as a function of fluence is a direct measure of the efficiency of the demagnetization process.

To make this argument more sound and in order to explore how far the spatially inhomogeneous excitation profile (see figure 2) and the metallic nanostructure influence the remagnetization dynamics, we have solved the TTM in two dimensions for our sample geometry. We assign heat capacities C, diffusion constants D, and temperatures T for the coupled baths of electron charge (e), lattice (l), and spin (s). After laser excitation of the electronic system, coupling to lattice and spin degrees of freedom leads to an increase of the spin temperature and hence to a loss of magnetization. More details of the calculation and all material parameters are summarized in the appendix. The spatial temperature distribution of electrons, T_e, lattice, T_l, and spins, T_s, at t = 300 fs is shown in figure 4(a). In spite of the strong reflectivity of the gold surface, the small specific heat of the electrons in gold results in high temperatures of the enhanced and localized excitation at the gold edges. The electron energy spreads very rapidly and homogeneously heats up the electronic system of the upper gold layer. Note that due to the large ballistic range of electrons in gold, the time scale of this process is likely to be underestimated in this calculation [19]. Because of a comparatively small electron–phonon coupling in gold, the electrons stay hot while the lattice remains relatively cool. Titanium, on the other hand, behaves very differently; its large value of $\Im(\epsilon)$ results in a strong absorption, whereas the large electron–phonon coupling constant leads to an efficient transfer of energy to the lattice. Furthermore, slow electron diffusion as well as a small mean free path of electrons in titanium effectively block hot electrons from the top gold layer from entering the magnetic layer. In combination with the small heat diffusion coefficient of titanium, this results in a very high and localized lattice temperature. In the magnetic film, regions of maximal spin temperatures are localized at the Ti/Au edges, as one would expect from the excitation profile shown in figures 2(a) and (b). After 300 fs, the strongly elevated spin temperature already extends several tens of nanometres under the Ti/Au lines. For even later times, further energy flow from the Ti layer into the magnetic film leads to a heating of the spin system of the Ti/Au-covered magnetic layer. (The temporal evolution of the TTM calculation is available as a supplementary data file.) At this point, it is worth noting that without the Ti layer the dynamics would be altered quite dramatically, as the very hot electrons from the top gold layer could reach the magnetic film unhindered, thus leading to an almost

Table 1. Experimental ratios of the slopes for structured and unstructured sample for s- and p-polarization and sample A and B (Enh_{theo}). Calculated ratios of the maximal $T_{s,avg}$ at $t = 300$ for structured and unstructured sample (Enh_{theo}).

sample	polarization	Enh_{exp}	Enh_{theo}
A	s	1.6 ± 0.5	1.3
A	p	0.6 ± 0.2	0.75
B	s	1.4 ± 0.8	1.4
B	p	0.4 ± 0.2	0.6

instantaneous increase of the electron and spin temperatures of the buried magnetic film. This is interesting, as in a recent experiment demonstrating the efficient demagnetization of gold-covered magnetic films [20], it was argued that this result points to an exclusively superdiffusive spin transport-driven demagnetization process. However, here we show that the TTM model incorporating electron diffusion is already able to account for non-local demagnetization dynamics.

The temperatures T_e, T_l, and T_s are integrated within the uncovered magnetic film (between the inplane distance $-100\ \text{nm} < x < 100\ \text{nm}$) and weighted with the exponential absorption profile of the $\lambda = 400$ nm probe light. Their temporal evolution for both the unstructured and structured sample are shown in figure 4(b). In order to reach the same maximum of the averaged spin temperature, the excitation fluence for the unstructured sample is scaled by a factor of 1.3; i.e., the simulation clearly predicts an enhanced demagnetization amplitude. For the same spin temperature the time evolution of the average spin temperatures $T_{s,avg}$ remains almost unchanged. Close inspection reveals a subtle increase of both τ_{de} and τ_{re} by 10 fs and 40 fs, respectively. These calculations are performed for both samples with s- and p-polarized excitation. Finally, it is worth noting that the calculations reproduce a linear increase of de- and remagnetization time constants as a function of fluence within the range of the experimental data [17].

The last step is to quantitatively compare the experimental results of the magnetization dynamics with the calculations described. We define the ratio of the slopes of τ_{re} as a function of fluence between the structured and unstructured samples Enh_{exp} as the experimental measure of the enhanced magnetization caused by the gold gratings. The calculations yield a maximal $T_{s,avg}$ at $t = 300$ fs for structured and unstructured samples; its ratio is denoted by Enh_{theo}. The values are summarized and compared in table 1 and show a very good agreement. We conclude that the demagnetization magnitude is significantly enhanced via the Ti/Au gratings when being excited with s-polarized light.

Finally, we examine the influence of the nanostructuring on the demagnetization rate. With a linear relationship between demagnetization time and excitation fluence, as predicted theoretically [17] and observed in previous experiments [17, 21], we plot in figure 5 the demagnetization time constant τ_{de} of sample A as a function of the corresponding remagnetization time constant τ_{re}. This relationship $\tau_{re}(\tau_{de})$ has the advantage to be independent of the explicit excitation fluence, in general susceptible to a large experimental error. The solid lines are linear least square fits. The extracted linear behaviour shows an almost identical slope but a small offset of approximately 40 fs. The shaded area depict a 35% confidence interval of the respective linear fits. This experimental evidence for a systematic acceleration of the demagnetization is too weak to make a strong claim regarding additional demagnetization channels in the presence of the metallic grating. The presence of such a channel may be expected in the light of the recent discussion regarding demagnetization by superdiffusive spin currents [6]. Nevertheless, we cannot exclude the following scenario: the strongly localized excitation at the edge of the metallic grating will allow more mobile majority spins of the magnetic film to superdiffusively enter the Ti/Au mask, while unpolarized electrons from the mask will compensate the electric charge within the Co/Pt multilayer, hence leading to an additional ultrafast demagnetization. As mentioned earlier, such a process has been experimentally and theoretically described in a recent publication [20] and may also play a role for our sample geometry. In future experiments one could tailor a more pronounced effect and, therefore, also a clearer experimental signature of super-diffusive transport effects by maximizing the surface boundary between magnetic and non-magnetic metals.

4. Conclusion

We have demonstrated that nanostructured metallic gratings on thin magnetic films can significantly enhance the amplitude of ultrafast demagnetization. We have established that the slope of the remagnetization time constants as a function of fluence is a reliable experimental measure to quantify the amplitude of the demagnetization for low noise measurements on complicated nanostructured samples. Our experimental

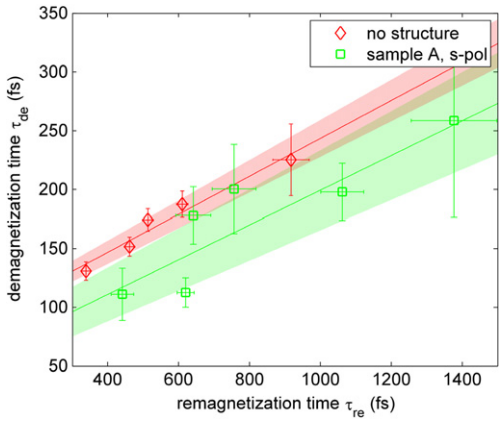

Figure 5. Extracted demagnetization time constants τ_{de} as a function of the corresponding remagnetization time τ_{re} for sample A. The solid lines are linear fits. One observes comparable slopes with a slight offset of approximately 40 fs. The shaded areas depict a confidence interval of 35%.

Table A1. Material constants used for the TTM calculations. Listed are the complex permittivity $\epsilon = \epsilon_1 + i\epsilon_2$ at $\lambda = 400$ nm and 800 nm, electron–phonon coupling constants g_{el}, electronic- and lattice-specific heat, as well as the heat diffusion coefficients at room temperature. For gold and titanium we use temperature-dependent values for $c_e(T, \vec{x})$ and $g_{el}(T, \vec{x})$ [22]. It is worth noting that the g_{el} of gold takes values between 3E16 [W/(m^{3}K)] and 14E16 [W/(m^{3}K)] in the temperature range of [300 K 10000 K]; i.e., it is significantly smaller than that of all other materials used.

		Co	Pt	Ti	Au
ϵ_1	($\lambda = 800$ nm)	−16.873 [23]	−16.449 [24]	6.207 [23]	−24.061 [25]
ϵ_2	($\lambda = 800$ nm)	23.897 [23]	28.362 [24]	25.200 [23]	1.507 [25]
ϵ_1	($\lambda = 400$ nm)	−6.229 [23]	−5.118[24]	−4.362 [23]	−1.658[25]
ϵ_2	($\lambda = 400$ nm)	9.315 [23]	9.844 [24]	12.362 [23]	5.735 [25]
g_{el}	[W/(m^{3}K)]	93E16 [19]	25E16 [19]	g_{el}(T)[22]	g_{el}(T) [22]
c_e	[J/(K^{2}m^3)]	704 T_e[26]	740 T_e [26]	c_l(T) [22]	c_l(T) [22]
c_l	[J/(m^{3}K)]	3.73E6 [26]	2.78E6 [26]	2.35E6 [26]	1.74E6 [26]
d_l	[W/(mK)]	100 [26]	72 [26]	22 [26]	318[26]

results agree with calculations showing a strongly localized excitation at the edges of the gold gratings and extending several nanometres into the magnetic film. The time- and space-dependent solution of the TTM in two dimensions for electron, lattice, and spin temperatures reveal non-local demagnetization dynamics depending sensitively on the sample materials and geometry. In particular, our observations are consistent with considerable demagnetization of the buried magnetic film due to electron diffusion. Finally, there is evidence of a subtle decrease of the demagnetization time constants for samples with metallic gratings, consistent with the notion of a secondary demagnetization channel based on super-diffusive spin transport.

Acknowledgments

We are thankful to M Schneider for recording the scanning electron microscope images of the metallic nanostructures. CvKS, StS, DW, and SE gratefully acknowledge support from the German Bundesministerium für Bildung und Forschung under contract no. 05K10KTB/FSP-301 (MPScatt).

Appendix: Three Temperature Model

For the time-dependent, two-dimensional calculation of the TTM, the following simplified system of partial differential equations of electrons, lattice, and spin was used.

$$c_e\left(T, \vec{x}\right)\frac{\partial T_e\left(\vec{x}\right)}{\partial t} + \nabla\left(-d_e\left(T, \vec{x}\right)\nabla T_e\left(\vec{x}\right)\right) = g_{el}\left(T, \vec{x}\right)\left(T_l\left(\vec{x}\right) - T_e\left(\vec{x}\right)\right) + S\left(t, \vec{x}\right) \qquad (1.1a)$$

$$c_{\mathrm{l}}\left(T,\vec{x}\right)\frac{\partial T_{\mathrm{l}}\left(\vec{x}\right)}{\partial t}+\nabla\left(-d_{\mathrm{l}}\left(T,\vec{x}\right)\nabla T_{\mathrm{e}}\left(\vec{x}\right)\right)=g_{\mathrm{el}}\left(T,\vec{x}\right)\left(T_{\mathrm{e}}\left(\vec{x}\right)-T_{\mathrm{l}}\left(\vec{x}\right)\right) \tag{1.1b}$$

$$\frac{\partial T_{\mathrm{s}}\left(\vec{x}\right)}{\partial t}=\frac{1}{\tau_{\mathrm{m}}}\left(T_{\mathrm{e}}\left(\vec{x}\right)-T_{\mathrm{s}}\left(\vec{x}\right)\right) \tag{1.1c}$$

where $c_{\mathrm{e}}(T,\vec{x})$, $d_{\mathrm{e}}(T,\vec{x})$ and $g_{\mathrm{el}}(T,\vec{x})$ are the space, and temperature-dependent coefficients of the specific heat, heat diffusion, and electron–phonon coupling, respectively. $\vec{x}$ depicts the two spatial coordinates of the simulation, the in-plane distance, x, and the height, z. The electronic heat diffusion is approximated by $d_{\mathrm{e}}(T,\vec{x})=d_{\mathrm{l}}\times(T,\vec{x})\,T_{\mathrm{e}}(\vec{x})/T_{\mathrm{l}}(\vec{x})$ [19]. Incorporation of electron diffusion results in non-local ultrafast demagnetization. These effects are expected to be particularly pronounced with gold, because its electrons have a large ballistic range on the order of 100 nm [19]. The source term S(t, $\vec{x}$) is the absorption profile shown in figure 2, and its temporal evolution is assumed to follow a Gaussian pulse with an FWHM of 120 fs.

Table A1 summarizes the used parameters for the different materials of our nano structure and of the magnetic Co/Pt multilayer.

References

[1] Malinowski G, Dalla Longa F, Rietjens J H H, Paluskar P V, Huijink R, Swagten H J M and Koopmans B 2008 Control of speed and efficiency of ultrafast demagnetization by direct transfer of spin angular momentum *Nat. Phys.* **4** 855–8

[2] Rudolf D, Chan L O and Battiato M 2012 Ultrafast magnetization enhancement in metallic multilayers driven by superdiffusive spin current *Nat. Phys.* **3** 1037

[3] Turgut E *et al* 2013 Controlling the competition between optically induced ultrafast spin–flip scattering and spin transport in magnetic multilayers *Phys. Rev. Lett.* **110** 197201

[4] Vahaplar K, Kalashnikova A, Kimel A, Hinzke D, Nowak U, Chantrell R, Tsukamoto A, Itoh A, Kirilyuk A and Rasing T 2009 Ultrafast path for optical magnetization reversal via a strongly nonequilibrium state *Phys. Rev. Lett.* **103** 117201

[5] Mangin S *et al* 2014 Engineered materials for all-optical helicity-dependent magnetic switching *Nature Mat.* **13** 286–92

[6] Battiato M, Carva K and Oppeneer P M 2010 Superdiffusive spin transport as a mechanism of ultrafast demagnetization *Phys. Rev. Lett.* **105** 027203

[7] Pfau B *et al* 2012 Ultrafast optical demagnetization manipulates nanoscale spin structure in domain walls *Nature Comm.* **3** 1100

[8] Vodungbo Boris *et al* 2012 Laser-induced ultrafast demagnetization in the presence of a nanoscale magnetic domain network *Nature Comm.* **3** 999

[9] von Korff Schmising C *et al* 2014 Imaging ultrafast demagnetization dynamics after a spatially localized optical excitation *Phys. Rev. Lett.* **112** 217203

[10] Challener W A 2009 Heat-assisted magnetic recording by a near-field transducer with efficient optical energy transfer *Nat. Photonics* **3** 220–4

[11] Pan L and David B B 2009 Data storage: heat-assisted magnetic recording *Nat. Photonics* **3** 189–90

[12] Kuiper K C, Malinowski G, Dalla Longa F and Koopmans B 2011 Nonlocal ultrafast magnetization dynamics in the high fluence limit *J. Appl. Phys.* **109** 07D316

[13] Lumerical Solutions, Inc. Vancouver, BC V6E 3L2, Canada

[14] Koopmans B 2007 Time-resolved Kerr-effect and spin dynamics in itinerant ferromagnets *Handbook of Magnetism and Advanced Magnetic Materials* (New York: Wiley) doi:10.1002/9780470022184.hmm313

[15] Atxitia U, Chubykalo-Fesenko O, Walowski J, Mann A and Münzenberg M 2010 Evidence for thermal mechanisms in laser-induced femtosecond spin dynamics *Phys. Rev.* B **81** 174401

[16] Kazantseva N, Nowak U, Chantrell R W, Hohlfeld J and Rebei A 2008 Slow recovery of the magnetisation after a sub-picosecond heat pulse *Europhys. Lett.* **81** 27004

[17] Koopmans B, Malinowski G and Dalla Longa F 2010 Explaining the paradoxical diversity of ultrafast laser-induced demagnetization *Nat. Mater.* **9** 259–65

[18] Cheskis D, Porat A, Szapiro L, Potashnik O and Bar-Ad S 2005 Saturation of the ultrafast laser-induced demagnetization in nickel *Phys. Rev.* B **72** 014437

[19] Hohlfeld J, Wellershoff S S and Güdde J 2000 Electron and lattice dynamics following optical excitation of metals *Chem. Phys.* **251** 237–58

[20] Eschenlohr A, Battiato M, Maldonado P, Pontius N, Kachel T, Holldack K, Mitzner R, Föhlisch A, Oppeneer P M and Stamm C 2013 Ultrafast spin transport as key to femtosecond demagnetization *Nat. Mater.* **12** 332–6

[21] Moisan N, Malinowski G, Mauchain J, Hehn M, Vodungbo B, Lüning J, Mangin S, Fullerton E E and Thiaville A 2014 Investigating the role of superdiffusive currents in laser induced demagnetization of ferromagnets with nanoscale magnetic domains *Scientific Reports* **4** 1–6

[22] Lin Z, Zhigilei L V and Celli V 2008 Electron–phonon coupling and electron heat capacity of metals under conditions of strong electron–phonon nonequilibrium *Phys. Rev.* B **17** 1–17

[23] Johnson P B and Christy R W 1974 Optical constant of transition metals: Ti, V, Cr, Mn, Fe, Co, Ni, and Pd *Phys. Rev.* **9** 5056–70

[24] Rakić A D, Djurišić A B, Elazar J M and Majewski M L 1998 Optical properties of metallic films for vertical-cavity optoelectronic devices *Appl. Opt.* **37** 5271–83

[25] Johnson P B and Christy R W 1970 Optical constants of the noble metals *Phys. Rev.* B **1318** 1972

[26] Gray D E 1972 *American Institute of Physics, Handbook* 3rd edn. (New York: Mc Graw Hill)